The electrical conductivity and photocatalytic activity of ultrafine iron hydroxide/oxide systems

Andrii B. Hrubiak, Volodymyr O. Kotsyubynsky, Volodymyr V. Moklyak, Bogdan K. Ostafiychuk, Pavlo I. Kolkovsky, Sofia V. Fedorchenko & Bogdan I. Rachiy

Published online: 07 Jun 2019.

Submit your article to this journal

Article views: 6

View Crossmark data

Taylor & Francis
Taylor & Francis Group

Check for updates

The electrical conductivity and photocatalytic activity of ultrafine iron hydroxide/oxide systems

Andrii B. Hrubiak[a], Volodymyr O. Kotsyubynsky[b], Volodymyr V. Moklyak[a], Bogdan K. Ostafiychuk[a], Pavlo I. Kolkovsky[b], Sofia V. Fedorchenko[b], and Bogdan I. Rachiy[b]

[a]Institute of Metal Physics, National Academy of Science, 36, ACad. Vernadsky Blvd., Kyiv, Ukraine; [b]Vasyl Stefanyk Precarpathian National University, 57, Shevchenko Str., Ivano-Frankivsk, Ukraine

ABSTRACT

The ultrafine iron hydroxide/oxide systems are fabricated by a hydrothermal approach, using iron nitrate and citric acid as precursors. The phase composition, crystal and magnetic microstructures, morphology, conductivity, and optical properties are characterized by X-ray diffraction, scanning electron microscope, impedance spectroscopy, Mössbauer spectroscopy, and UV-VIS spectroscopy. The mechanisms of phase transformation of amorphous ultrafine γ-FeOOH$\rightarrow$ nanocomposite γ-Fe$_2$O$_3$/α-Fe$_2$O$_3$ in the temperature interval 150–350°C are established. The photocatalytic activity of samples was estimated by the degradation of methylene blue and formaldehyde under UV or visible light in an aqueous solution. The results indicate that the photocatalytic degradation activities of amorphous γ-FeOOH and nanocomposite γ-Fe$_2$O$_3$/α-Fe$_2$O$_3$ are higher than that of phase pure γ-Fe$_2$O$_3$. The photocatalytic property of samples is related to their conductivity and band gap. This implies that a synergistic effect exists between the conductivity and the photocatalytic activity in the ultrafine iron hydroxide/oxide systems. In addition, it can be attributed to the active heterogeneous Fenton process for γ-FeOOH and the microstructure of γ-Fe$_2$O$_3$/α-Fe$_2$O$_3$, which is probably caused by a successful combination of electronic structures of the phases of magnetite and hematite.

1. Introduction

In many cases, the chemical production is accompanied by significant environmental threats due to the generation and accumulation of harmful industrial waste. Therefore, the improvement of the methods of utilization of pollutants is an urgent scientific social problem. In recent years, the treatment of organic waste water is one of the most urgent subjects in the pollution control because of its high concentration and refractory degradation [1]. There are many methods (physical, chemical, and biological) for the industrial waste cleaning from organic toxins and carcinogens, but the problems to increase their efficiency and to reduce costs remain actual. Semiconductor photocatalysis is one of the advanced physico-chemical processes applicable in the photo-degradation of

---

environmental organic pollutants and toxins due to the simplicity, environmental safety, and low cost [2]. The efficiency of heterogeneous photocatalysts depends on the physical and chemical properties of semiconducting active materials. They are typically more productive and stable in the oxidation/reducing processes as compared with molecular catalysts. TiO_2 is the most common and studied heterogeneous photocatalyst, but its relatively large band gap (E_g = 3.0-3.3 eV) limits the application of the material by the ultraviolet part (about 7%) of the solar spectrum [3]. Thus, the development of an effective photocatalyst adapted to the visible range of solar radiation is the actual problem. The photocatalyst based on iron oxides and hydroxide is promising from this point of view. The advantages of these materials are the environmental stability, low cost, and comparatively narrow band gap (about E_g = 2.0-2.2 eV [4]). The photocatalytic activity of iron compounds can be improved, by using ultrafine and mesoporous materials with modified morphology of particles. At the application of lepidocrocite γ-FeOOH as a photocatalyst, its tunnel structure presents the additional advantage for improving the photocatalytic activity in comparison with different polymorphic modifications of iron oxides [5–7]. In addition, the issues of the influence of the conductivity on the photocatalytic activity of iron compounds are very interesting. The combination of the good conductivity, porous structure, and high specific surface area allows a rapid charge transfer pathway, excellent light trapping, and increasing the reaction sites [8].

The aim of this work was to investigate the influence of the phase composition, structure, morphology, conductivity, and optical properties of synthesized materials on their photocatalytic activity.

2. Materials and methods

2.1. Synthesis of materials

The ultrafine iron hydroxide/oxide systems were fabricated by the hydrothermal approach, by using iron nitrate and citric acid as precursors. On the first stage, iron citrate sol was obtained by a slow mixing of 0.4 M $Fe(NO_3)_3 \cdot 9H_2O$ and $C_6H_8O_7 \cdot H_2O$ aqueous solutions (molar ratio 1:1) at 50°C for 1 h. Final pH of iron citrate sol is 0.3. On the next stage, the formed sol of iron citrate was treated in a hydrothermal reactor at a temperature of 120°C for 20 h. After that, an orange precipitate powder was washed in distilled water to pH =7 with the next aging at 60°C in air for 24 h. A dried precipitate powder (sample G1) was annealed at 150°C (sample G2), 250°C (sample G3), and 350°C (sample G4). XRD, Mössbauer spectroscopy, electron microscopy, low-temperature nitrogen adsorption, optical and impedance spectroscopies were used for the analysis of physical and chemical properties of materials.

2.2. Structure, morphology, electrical and optical properties

The phase composition and diffraction patterns were investigation, by using a DRON-2.0 X-ray diffractometer (Cu K_α radiation). The Bragg–Brentano geometry and a Ni K_β-filter were used. A qualitative analysis was carried out through ICSD structural models. A copper powder annealed in vacuum (850 – 900 °C for 4 h) with an average grain size of about 50 μm was used as a reference sample for the determination of the

instrumental peak broadening. The full width at half maximum (FWHM) for a diffraction peak of this reference sample at $2\theta = 43.38°$ was $0.129°$. The size of coherently scattering domains was calculated by the Scherrer equation:

$$D = \frac{k\lambda}{\beta \cos \theta} \tag{1}$$

where k is the Scherrer constant ($k = 0.9$), λ is the wavelength (0.15405 nm), β the FWHM (in radians), and θ is the peak angular position. As a profile shape, we used a combination of Gauss and Cauchy (dominated) functions.

The electrical conductivity σ as a function of the frequency was measured by the impedance spectroscopy in the frequency range 0.01–100 kHz, by using an Autolab PG-STAT 12/FRA-2 analyzer. All samples were made in the pellet form with a diameter of $17 \cdot 10^{-3}$ m and a thickness of $0.1 \cdot 10^{-3}$ m under a pressure of about 33-35 MPa at room temperature.

The investigations of the morphology for synthesized materials were carried out, by using scanning electron microscopy (JEOL JEM-100CX II). The specific surface areas (BET) and pore size distribution were measured by low-temperature nitrogen adsorption/desorption methods at 77 K with a Quantachrome NOVA 2200e analyzer.

The Mössbauer spectra were measured at room temperature with an MS-1104em spectrometer (^{57}Co source, FWHM for α-Fe spectra was about 0.29 mm/s). The isomer shifts (δ) and quadrupole splitting (Δ) were measured relative to α-Fe. The model fitting was performed using the Univem MS-701 softaware.

The optical transmittance spectra of samples were measured by a UV-VIS Spectrophotometer USB 2000 Fiber Optic Spectrometer in the wavelength interval 200-800 nm. The value of the band gap can be determined, by using the formula

$$\alpha = \frac{const}{h\nu} \left[h\nu - E_g \right]^m. \tag{2}$$

Here, α – the absorption coefficient, E_g – band gap, h – Planck constant, ν – the photon frequency, m is a constant depending on the type of electronic transition ($m = 1/2$ and 2 for direct and indirect transitions, respectively).

2.3. Photocatalytic measurements

The degradation of aqueous solutions of MB dye and formaldehyde under the influence of visible and UV light irradiation was used for testing the photocatalytic activity of synthesized materials. MB as one of the azo dyes, which are the typical industrial effluents in a good model for the study of photocatalytic properties of iron oxide systems. The formaldehyde and its derivatives are used in the production of polymeric materials, polyhydric alcohols, and isoprene. It is one of the main organic pollutants. The photocatalyst was introduced as a suspension into a aqueous solutions in a thermostated photochemical quartz reactor. As a source of visible UV light irradiation, we used a InfoLight H1 50W Xenon and 26 W EBT-01 halogen lamps. A Corning K-glass filter was used to avoid the heating of the solutions.

The photocatalytic degradation occurs on the surface of particles. So, the studies of the adsorption of the MB dyes from aqueous solutions onto iron oxide particles are of
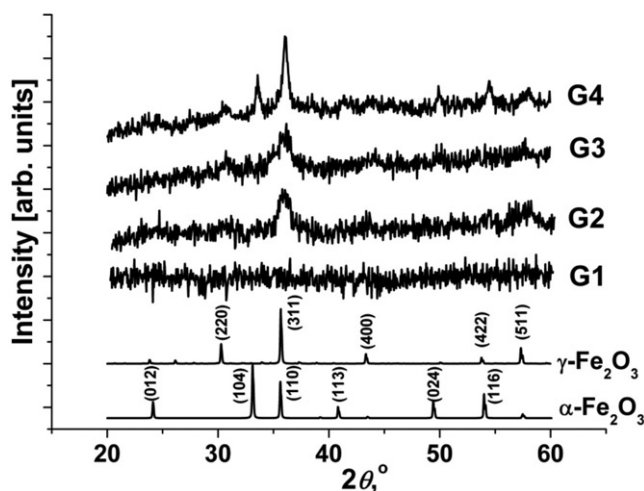
Figure 1. X-ray diffraction patterns of synthesized iron hydroxide and oxide samples

importance. The addition of synthesized materials to an aqueous solution of MB in dark for 5h showed no decrease in the dye concentration, which indicates that there occurs no adsorption of the dye on the catalyst. Therefore, the initial concentration was taken to be C_0 itself in all the cases. Blank experiments were also carried out for the MB and formaldehyde without a catalyst degraded by direct UV and visible radiation. After checking that there is no degradation with irradiation alone, the photocatalytic degradation was studied.

The sample (150 mg) was added to the 15-ml MB aqueous solution (initial concentration $C_0 = 40$ mg/l) and mixed with a magnetic stirrer in dark for about 60 min up to the adsorption/desorption equilibrium. At the next stage, 5 ml of a 35% H_2O_2 solution were added to the suspension and were irradiated with UV at a constant stirring for 30 min. After that, the samples (6-8 ml) of solutions were taken from a photocatalytic reactor at different stages of the decolorization and centrifuged for 20 min at a frequency of 8000 rpm for the separation of an iron oxide powder.

The films of iron oxide/hydroxide samples (40-50 μm in thickness, 6 cm^2 in area) on the K-glass substrates were used to investigate the formaldehyde aqueous solution photodecomposition. The initial concentration of formaldehyde was 0.40 mg/l. The photocatalyst film was immersed in a formaldehyde solution and irradiated for 10 min.

A "ULAB 102 UV" UV/VIS spectrometer recording the spectra over the 190–750-nm range was used for the determination of MB and formaldehyde concentrations to follow their kinetics of disappearance. The calibrations based on the Beer–Lambert law were linear and used to quantify the concentration of dyes. The normalized concentration changes (C/Co) of dyes during the photodegradation are proportional to the maximum absorbance and derived from the changes in dye's absorption profile (670 nm for MB and 414 nm for formaldehyde).

The photocatalytic properties of the synthesized materials has been investigated with the use of the analysis of kinetic characteristics of the photocatalyst process, namely, the rate constant of the reaction (K) and the half-life time ($t_{1/2}$). The equations for kinetic characteristics of the photocatalysis are presented below:
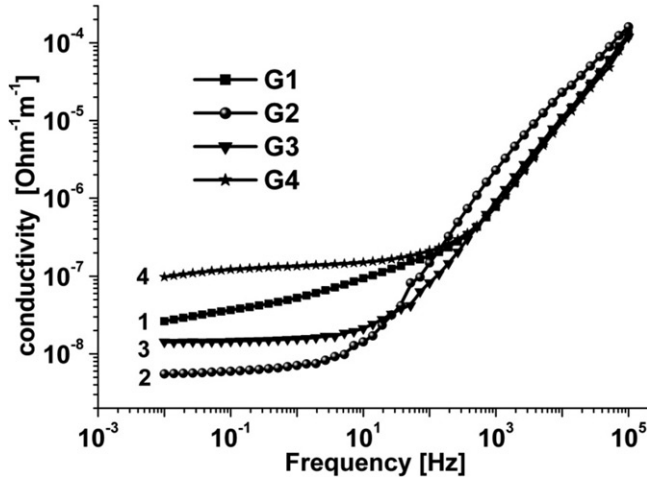
Figure 2. Frequency dependences of the ac conductivity of iron hydroxide and oxide samples obtained at the different annealing temperatures

$$C = C_0 \exp\left(-Kt\right), \tag{3}$$

$$K = \frac{1}{t}\ln C_0/C, \tag{4}$$

where C_0 is the initial concentration of an organic pollutant in the solution; C is concentration at the time

$$t_{1/2} = \frac{1}{K}\ln\frac{C}{C_0} = \frac{\ln 2}{2} = \frac{0.693}{K}. \tag{5}$$

3. Results and discussion.

According to XRD data, G1 sample is close to the amorphous one, since there are no peaks on the XRD pattern (Fig. 1).

Annealing of G1 sample at 150 °C for 2 h (sample G2) causes the crystallization of the material and the ultrafine γ-Fe$_2$O$_3$ formation (Fig. 1) with the average sizes of the coherent scattering region (CSR) about 6 nm. The material obtained after the annealing at 250 °C (sample G3) has no change in the phase composition and crystalline structure compared to G2 sample; the average CSR size is about 6 nm. The particle size is determined by taking the average of the sizes at peaks (220), (311), (400), (422), and (511). The beginning of the γ-Fe$_2$O$_3$ $\rightarrow$ α-Fe$_2$O$_3$ phase transformation for the material annealed at 350 °C (sample G4) was observed (γ-Fe$_2$O$_3$/α-Fe$_2$O$_3$ ratio is 65/35) The increasing of the average CSR size for the γ-Fe$_2$O$_3$ phase up to 11 nm was established, while the CSR size for the α-Fe$_2$O$_3$ phase was about 26 nm. The particle size of α-Fe$_2$O$_3$ is determined by taking the average of the sizes at peaks (012), (104), (110), (024), and (116).

The values obtained for samples G2 and G3 can be attributed to the simultaneous formation of another phase such as Fe$_3$O$_4$ (JCPDS Card No. (79-0417)). The diffraction pattern of the defective spinel γ-Fe$_2$O$_3$ differs from that of the inverse spinel Fe$_3$O$_4$ by

the appearance of weak additional reflexes (111), (222), and (511) and due to the regulation of oxygen vacancies in the octahedral positions of the structure of γ-Fe$_2$O$_3$ [9]. In addition, crystallographically isomorphous maghemite and magnetite are differentiated by the presence of Fe^{2+} ions in the latter. The difference between the phases of γ-Fe$_2$O$_3$ and Fe$_3$O$_4$ is revealed in their electronic structure and, accordingly, electroconductivity properties. The band gap for maghemite is 2.06 eV [10], whereas it is only 0.1 eV for magnetite [11]. Therefore, the specific conductivity of Fe$_3$O$_4$ is 1-10 Ohm^{-1}·m^{-1}, whereas, for γ-Fe$_2$O$_3$, it has a value lower by 7-8 orders [12].

For this reason and for the study of the electrical properties of synthesized materials, we carried out the impedance measurements and determined their electroconductivity. The experimental frequency dependence of the conductivity $\sigma(\omega)$ (Fig. 2) is typical of semiconductor materials with a percolation mechanism of conduction.

The approximation of the dependences $\sigma(\omega)$ was carried with the use of the Jonscher equation [13], which involves charge transfer mechanisms of non-Debye relaxation in the solid state:

$$\sigma(\omega) = \sigma_{dc} \cdot \left[1 + (\omega/\omega_h)^s\right], \tag{6}$$

where σ_{dc} is the conductivity in the direct current mode, ω_h is the charge jump frequency, s is the index characterizing a deviation of the system from the properties provided by the Debye model and is the measure of the interparticle interaction ($0 < s < 1$).

The frequency-independent component of the conductivity σ_{dc} at low frequencies for all samples varies in the range 10^{-7}–10^{-9} Ohm^{-1}·m^{-1} according to the analysis of obtained data. So, we can assert the formation of ultrafine maghemite at annealing temperatures 150°C and 250°C for samples G2 and G3.

At the same time, the analysis of the dependence $\sigma(\omega)$ was conducted. The parameter s in all cases is near the value $s \geq 1.0$, which indicates the equivalence of the character of the multiposition jumps of charge carriers due to an increase in the degree of homogeneity of the system. In this case, $\sigma(\omega)$ obeys the superlinear power law. Therefore, the conductivity spectra can be described by the modified Jonscher equation

$$\sigma(\omega) = \sigma_{dc} \cdot \left[1 + (\omega/\omega_h)^s + (\omega/\omega_n)^m\right], \tag{7}$$

where ω_h is a temperature-dependent parameter with $m > 1$ for the superlinear power law. The first term σ_{dc} in Eq. (7) is the well-known dc conductivity arising from the unrestricted random hopping of ions, the second is the Jonscher's power law arising due to the restricted ion hopping, and the third is the superlinear power law, due to two-level systems or low-energy excitation modes of vibrations [14]. In approaching the superlinear power law, the parameter s is within 0.85-0.95 for all samples, and the parameter m is within 1.15-1.27.

For G1 sample in the low-frequency region, a monotone linear change of the component σ_{dc} with the frequency is observed. This effect is probably due to the potentially complex processes of percolation diffusion of electrons on the defect structure of the X-ray amorphous material and the effects associated with the contribution of the impurity conductivity of the surface-adsorbed groups.

Annealing at 150°C causes abrupt structural changes in the material, which also affects electrical properties, namely, the specific electrical conductivity of the sample decreases. The least value of σ_{dc} for G2 is due to, probably, a high degree of dispersion
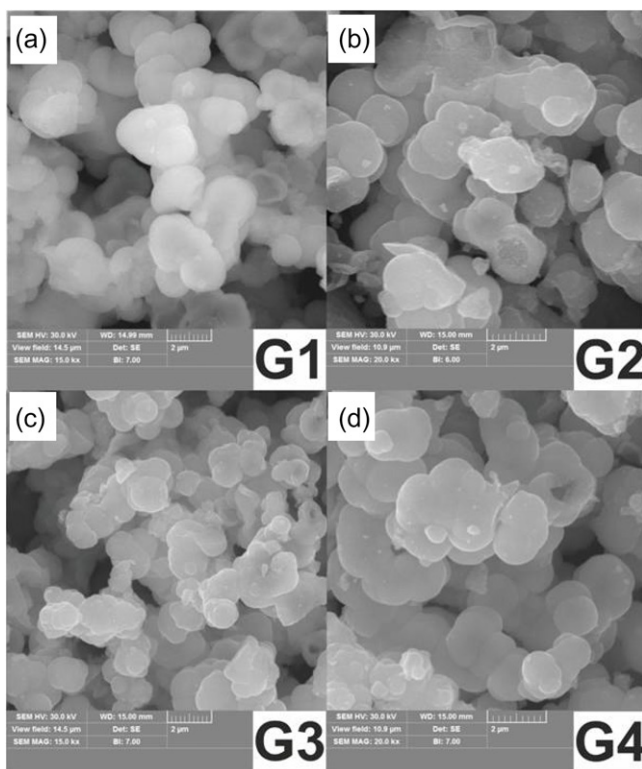
Figure 3. SEM images of iron hydroxide and oxide samples obtained at the different annealing temperatures

of the crystalline phase γ-Fe$_2$O$_3$ (the CSR size is 6 nm). As a result, an increase in the number of boundaries of the section is observed, which leads to an increase in the potential barrier height in the electronic structure of a material.

For G3 sample, we observed an increase in the frequency-independent component of the conductivity, which is caused by an increase in the specific surface area of the material and, as a result, the sharp increase in the surface diffusion. The further annealing at a temperature of 350 °C (G4 sample) causes an increase in the specific conductivity of the material due to increasing the degree of crystallinity of the material. In addition, an increase in the conductivity for G4 sample is due to the phase transformation γ-Fe$_2$O$_3 \rightarrow \alpha$-Fe$_2$O$_3$.

Moreover, it has been established that an increase in the annealing temperature causes the increase in the frequency, at which the transition of the independent component/the dependent component of conductivity occurs. This effect is due to a structural ordering of materials with increasing the annealing temperature. The dependence of this type is characteristic of the case of conductivity of materials, which are arranged at the microscopic level [15].

According to the SEM observation, G1 sample is formed by irregular spherical agglomerates (average size is about 3 μm) (Fig. 3, a). G2 and G3 samples (Fig. 3, b-c) have the high dispersion and porosity (average agglomerate sizes are 1-2 μm) due to the phase transformation and the desorption of water. G4 sample is characterized by
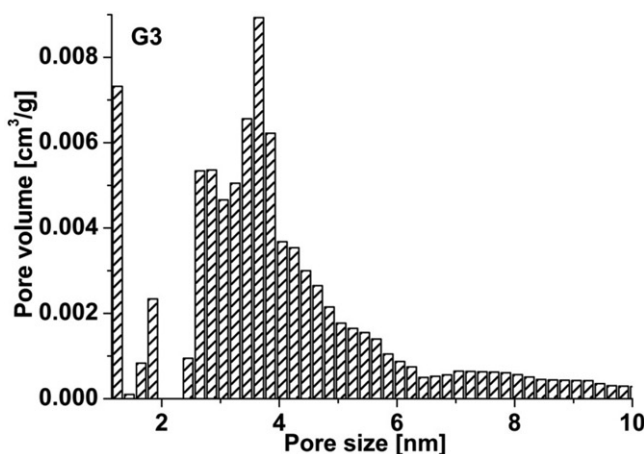
Figure 4. Pore size distribution for G3 sample

enlarging the sizes of particles caused by the phase transformation $\gamma\text{-}Fe_2O_3 \rightarrow \alpha\text{-}Fe_2O_3$ and the aggregation of particles due to their sintering (Fig. 3, d) .

This result is confirmed by the adsorption porometry. The initial G1 sample was low-porous with a specific surface area of about 20 m^2/g. The annealing at 150 C initiates the formation of $\gamma\text{-}Fe_2O_3$ with the specific surface area of about 45 m^2/g as a result of the gas evaporation. An increase in the annealing temperature (G3 sample) causes the material dispergation intensification and the increase in the specific surface area up to 97 m^2/g without phase changes. The sizes of pores for G3 sample are mostly concentrated in an interval of 2.5-6.0 nm with the maximum at about 4 nm; and the relative content of micropores (<2 nm) does not exceed 7% (Fig. 4). An increase in the annealing temperature up to 350 °C causes the $\gamma\text{-}Fe_2O_3 \rightarrow \alpha\text{-}Fe_2O_3$ phase transformation, which is accompanied by the maghemite particle sintering and a decrease in the specific surface area down to 35 m^2/g.

Mössbauer spectroscopy allows one to refine the phase composition and magnetic microstructure of synthesized samples. The Mössbauer spectrum of G1 sample is a result of the resonance absorption of γ-quanta by Fe^{3+} nuclei in the paramagnetic state (Fig. 5, a). The spectrum was optimally approximated by a superposition of two doublet components (Table. 1). The obtained isomeric shift (δ) and quadrupole splitting (Δ) are consistent with the parameters for the FeOOH phase. Unfortunately, the positive identification of each of the β-FeOOH and γ-FeOOH phases is impossible at 300K due to their nearly identical spectra [16]. The difference between the spectra of β-FeOOH and γ-FeOOH are manifested at low temperatures. β-FeOOH has magnetic order at a temperature below 90 K, and the spectrum consists of a sextet due to several magnetically inequivalent sites of Fe-ions. Hydroxide γ-FeOOH is paramagnetic at the low temperature. Therefore, we have removed the Mössbauer spectrum of G1 sample at a temperature of 90° (Fig. 5, b). G1 sample remains paramagnetic at low temperatures, and its spectrum is approximated by two doublet lines. The parameters of doublets finally indicate the γ-FeOOH for G1 sample [16]. The value of Δ is larger for the sample G1, than the previously fixed data for the bulk γ-FeOOH. This is due to the defective amorphous structure of the sample, where Fe^{57} nuclei occupy the non-equivalent positions in the crystal [17].
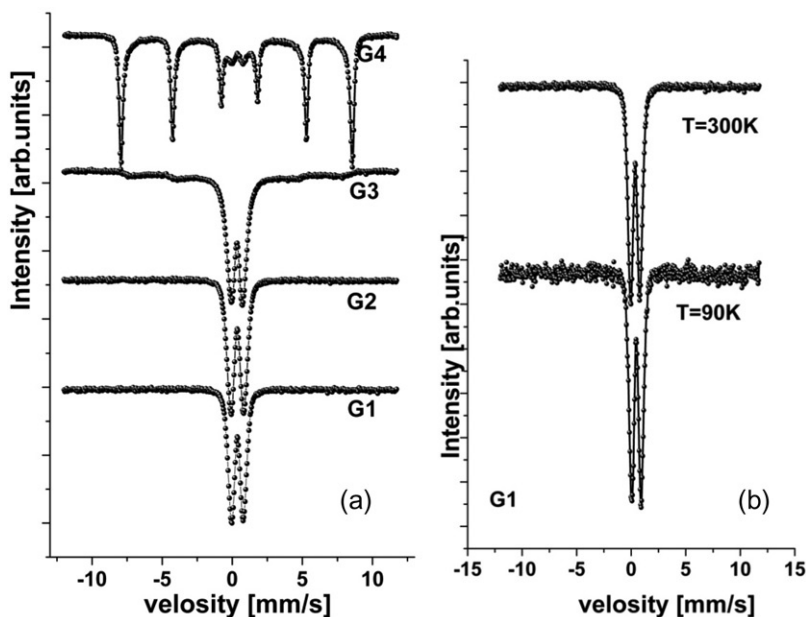
Figure 5. Mössbauer spectra of iron hydroxide and oxide samples

Table 1. Parameters of components of the Mössbauer spectra for synthesized samples

Sample	Phase	Components	δ, mm/s	Δ, mm/s	ω, mm/s	H_{eff}, kE	S, %
G1	γ-FeOOH	doublet No. 1	0.36	0.73	0.45	–	57
		doublet No. 2	0.37	1.14	0.58	–	43
G1, 90 K	γ-FeOOH	doublet No. 1	0.48	0.76	0.45		56
		doublet No. 2	0.47	1.16	0.65		44
G2	γ-Fe$_2$O$_3$	doublet No. 1	0.36	0.77	0.49	–	52
		doublet No. 2	0.36	1.25	0.64	–	48
G3	γ-Fe$_2$O$_3$	doublet No. 1	0.34	0.65	0.42	–	20
		doublet No. 2	0.32	1.05	0.70	–	44
		sextet No. 1	0.37	−0.06	1.85	449	36
G4	γ-Fe$_2$O$_3$	doublet No. 1	0.36	0.83	0.65	–	10
		sextet No. 1	0.37	−0.21	0.3	513	60
	α-Fe$_2$O$_3$	sextet No. 1	0.38	−0.11	0.77	483	30

The doublet component is dominating for the spectra of G2 and G3 samples. For G3, we see a wide weak sextet component, which corresponds to Fe^{3+} in a state close to the magnetic ordered one (Fig. 5, a). Comparing XRD with Mössbauer data for these samples, we can predict the superparamagnetic state of γ-Fe$_2$O$_3$ with the sizes about 5-6 nm [18]. The paramagnetic component in both cases has been approximated by two doublets with close values of the isomer shift (corresponding to Fe^{3+} ions in a high-spin state) and different values of the quadrupole splitting (Tabl. 1). The quadrupole splitting is determined by the symmetry of Fe^{57} nuclei near surroundings, so the two doublets can be explained by the presence of two non-equivalent positions of Fe^{3+}. The values of δ and Δ for the first doublet component match with the data for γ-Fe$_2$O$_3$ nanoparticles in the superparamagnetic state [19]. An increasing in the quadrupole splitting for the second doublet line means a decrease in the symmetry of the surroundings of Fe^{3+} ions [20].

Interpreting the results, we can suggest a core-shell structure of γ-Fe_2O_3, where doublet No. 1 corresponds to the inner part, and doublet No. 2 to the superficial defect layers of nanoparticles. This assumption is proved by comparing of the low-temperature nitrogen adsorption data and the relative content of paramagnetic components in Mössbauer spectra. The increase in the specific surface area for G3 sample to 97 m^2/g corresponds to a decrease in the first doublet component integral intensity (Tabl. 1), which indicates a decrease in the relative content of Fe^{3+} ions at core layers. In addition, the integral intensity of the second doublet remains unchanged, which indicates an increase in the relative number of iron nuclei in the shell layer.

The Mössbauer spectrum of G4 sample consists of a sextet part and a small paramagnetic component, which indicates the dominance of particles in the magnetic order state at room temperature (Fig. 4). The spectrum of G4 sample was approximated by two sextets, which correspond to the γ-Fe_2O_3 and α-Fe_2O_3 phases. The small paramagnetic doublet component (10%) corresponds to Fe^{3+} ions in a high-spin state. The ratio of the integral intensities of sextet components for both phases (Tabl. 1) is very close to that of the contents of the γ-Fe_2O_3 and α-Fe_2O_3 phases determined by XRD.

The investigation of the optical properties of synthesized materials by optical photospectroscopy provided information about the type of optical transitions and the bandgap energy. The measurement of transmission spectra was performed at room temperature in the 300-800-nm interval of wavelengths.

The spectra obtained with the use of the energy as the abscissa show that the bandgaps of all samples have only direct transitions (Fig. 6). The plots of $(ah\nu)^2$ were drawn to observe the direct gap of synthesized materials. The extrapolation of the linear part on the plots $(\alpha h\nu)^2(h\nu)$ to the abscissa allows us to find the energy gap values.

The band gap for G1 sample (amorphous γ-FeOOH, according to Mössbauer spectroscopy data) is about 2.34 eV (Fig. 6, a). The optical band gap for γ-FeOOH in the case of direct transitions is 2.0 eV [21]. Respectively, a higher value of the bandgap energy in our case for G1 sample can be associated with the ultrafine state of the material and quantum confinement effects [22].

Bandgap energies of 2.84 and 2.89 eV were calculated for G2 and G3 materials (γ-Fe_2O_3), respectively. This result is expected due to the dispergation of the material after the sintering at 250 °C. The typical bandgap energy for bulk maghemite is 2.03 eV [10]. In this case, the increase in the band gaps of G2 and G3 is compared with that of bulk γ-Fe_2O_3 caused by the quantum confinement. An insignificant increase in the band gap for G3 can be related to the dispergation of the material after the sintering at 250 °C and the reconstruction effects on the surface of γ-Fe_2O_3 nanoparticles. The band gap for G4 sample decreases down to 2.08 eV at the expense of a phase transformation of the material.

The photocatalytic activity of synthesized materials was appreciated as the degradation profile of MB and formaldehyde in water under the illumination with UV and visible light (Fig. 7).

In our case, the process of photocatalytic degradation of organic compounds with participation of oxide semiconductor phases of iron oxide/hydroxide can be schematically represented as follows [23]:
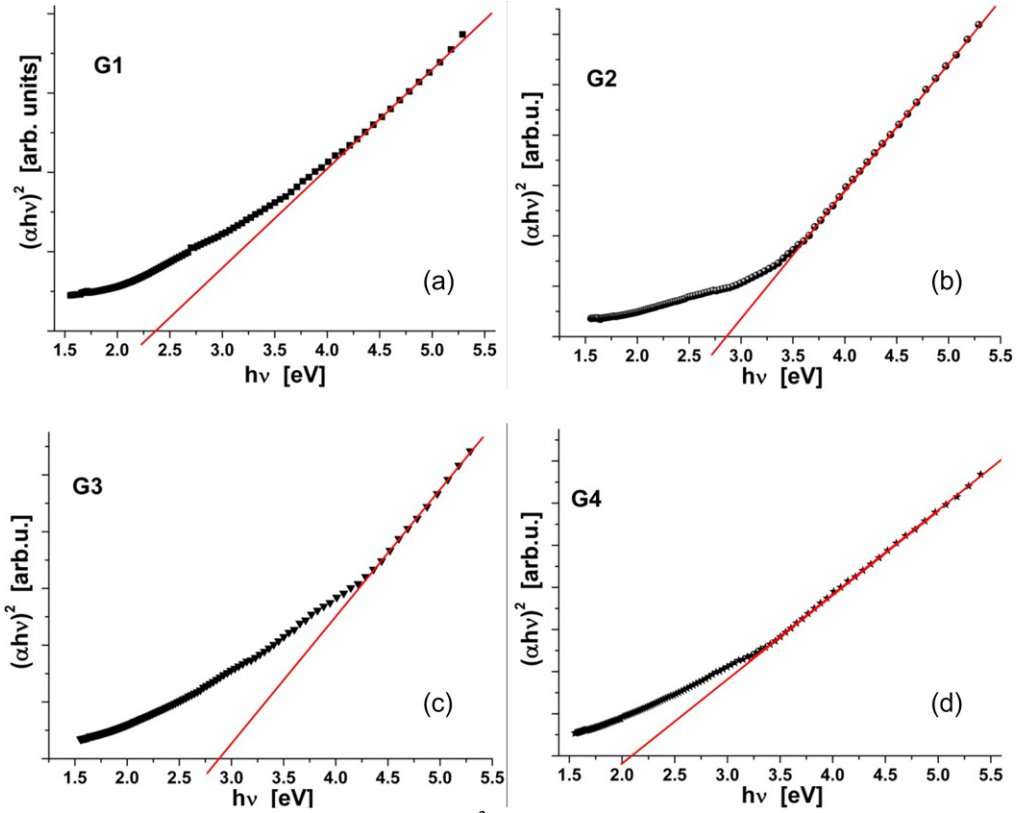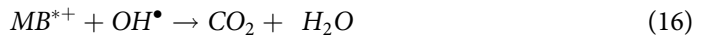
$$SC + \ h\nu \rightarrow SC(h^+ + e^-) \tag{8}$$

Figure 6. Plots of (ahν)2 versus (hν) for synthesized materials

$$h^+ + OH^- \rightarrow OH^\bullet \tag{9}$$

$$e^- + O_2 \rightarrow O_2^- \tag{10}$$

$$O_2^- + H^+ \rightarrow HO_2 \tag{11}$$

$$2HO_2 \rightarrow H_2O_2 + O_2 \tag{12}$$

$$H_2O_2 + e^- \rightarrow OH^- + OH^\bullet \tag{13}$$

$$MB \xrightarrow{h\nu} MB^* \tag{14}$$

$$MB^* + SC \rightarrow MB^{*+} + SC^- \tag{15}$$

$$MB^{*+} + OH^\bullet \rightarrow CO_2 + H_2O \tag{16}$$

Electrons and holes are continuously generated, when the solar light illuminates the surface of mixed metal oxide. The metal oxide containing surface hydroxyl groups (OH^-) is directly attacked by a hole to generate the $OH^\bullet$ radicals, whereas peroxide (O_2^-) is formed, when an electron reacts with dissolve oxygen present in the medium (water). This peroxide takes one proton to yield a superoxide (HO_2) followed by the formation of hydrogen peroxide (H_2O_2). Hydrogen peroxide again can split to give a hydroxide radical and a hydroxyl ion. The degradation of organic dyes is mainly due to the action of $OH^\bullet$ radicals on an organic molecule. This translates a molecule into an excited state and subsequently causes its destruction as the photocatalytic effect [24].
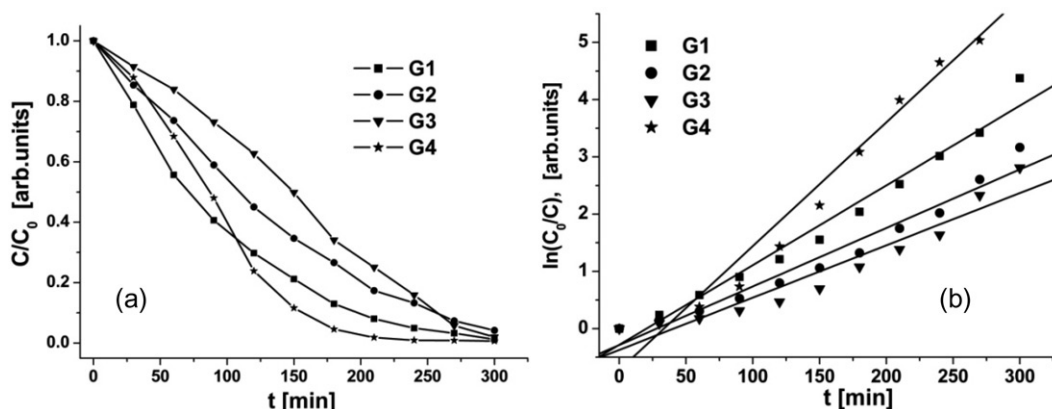
Figure 7. Photocatalytic degradation performance of methylene blue dye (a) and photocatalytic decomposition as a function of the irradiation time (b).
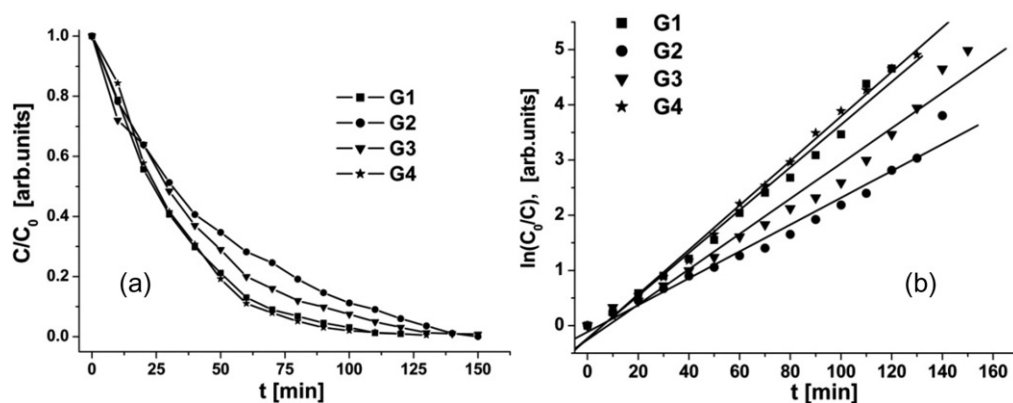

Figure 8. Photocatalytic degradation performance of formaldehyde (a) and photocatalytic decomposition as a function of the irradiation time (b).

The photocatalytic degradation performances of MB dye and formaldehyde were shown in Figs. 7 and 8, respectively.

The initial degradation reaction rates are determined by conducting a series of concentration versus time experiments. The maximum photocatalytic activity was observed for G1 and G4 samples. The times of the MB full decomposition were about 210 and 180 min for G1 and G4 samples, respectively. These samples have maximal activity in a case of formaldehyde photodegradation. According to experimental results, the photodegradation is described by the first-order reaction law.

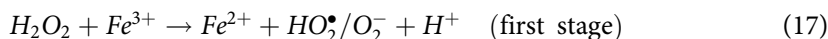The kinetic parameters of the photocatalytic decomposition of MB dye and formaldehyde were given in Table 2.

The high performances of the photodestruction of MB and formaldehyde demonstrated by G1 system are caused by γ-FeOOH phase peculiarities related to the Fenton process.

The photo Fenton reactions occur simultaneously with the photocatalytic process (the formation of electron-hole pairs under irradiation). The photo Fenton reaction is

Table 2. The kinetics parameters of photocatalytic decomposition.

No.	Sample	Degradation material	K, min^{-1}	$t_{1/2}$, min
1	G1	MB dye	0.015	46.20
		formaldehyde	0.038	18.24
2	G2	MB dye	0.009	77.00
		formaldehyde	0.024	28.88
3	G3	MB dye	0.010	69.30
		formaldehyde	0.031	22.35
4	G4	MB dye	0.022	31.50
		formaldehyde	0.040	17.33

associated with the formation of free hydroxyl radicals OH$^{\bullet}$ due to oxidation-reduction reactions involving iron ions $Fe^{3+} \leftrightarrow Fe^{2+}$ [25]. The formation of OH$^{\bullet}$ radicals is a result of the interaction between iron hydroxide and H_2O_2 under UV irradiation accordingly to the following chain reactions [26]:

$$H_2O_2 + Fe^{3+} \rightarrow Fe^{2+} + HO_2^{\bullet}/O_2^- + H^+ \quad \text{(first stage)} \tag{17}$$

$$H_2O_2 + Fe^{2+} \rightarrow Fe^{3+} + OH^- + OH^* \quad \text{(second stage)} \tag{18}$$

The concentration of OH$^{\bullet}$ radicals is crucial for the photocatalyst performance. The formation of OH$^{\bullet}$ species is also possible due to the destruction of H_2O_2 molecules at the capture of electrons or under irradiation. But the probability of these processes is less comparatively to that of $Fe^{3+} \leftrightarrow Fe^{2+}$ redox reactions.

The photoactivity for G2 and G3 samples (ultrafine magnetite) is comparatively lower than for G1 sample. In fact, the photodegradation based on ultrafine γ-Fe$_2$O$_3$ has gone worse compared to γ-FeOOH. At the same time, the kinetic characteristic of the photocatalytic degradation of G3 sample is better than for G2 sample: increase in the rate of degradation is observed in the transition from G2 sample to G3. The improvement of the photocatalytic properties of G3 sample is probably due to a high value of the surface area (97 m^2/g) [26].

In the case of the G4 material (γ-Fe$_2$O$_3$/α-Fe$_2$O$_3$ composite), the high photocatalytic activities for MB and formaldehyde are probably caused by a successful combination of electronic structures of the phases of maghemite and hematite. This effect improves the transport of generated electron-hole pairs and, as a result, leads to an increase in the photodegradation rate. The bandgap energies of maghemite (2.03 eV) [10] and hematite (2.02 eV) [27] are very close. but they has different energy positions of the valence and conduction bands. In hematite, the bands of conduction and valence are -0.62 eV and 1.40 eV, respectively, whereas they are -0.12 eV and 1.94 eV for magnetite, respectively [27]. Thus, in the γ-Fe$_2$O$_3$/α-Fe$_2$O$_3$ composite, the electrons from the conduction band of magnetite move into the conduction band of hematite, which causes the effective separation of electrons and their transport to the surface. As a result, the active reactive radicals OH are produced, which results in the higher photodegradation rate of MB.

There are several parameters that can influence the γ/α transition. They are the intergranular diffusion, specific surface area, and critical size of the system [28]. The most probable transition way is a size-depending germination–growth mechanism. The particles with the sizes smaller than 9 nm would be transformed first. But, in the volume of larger particles, the phase transition would be non-quasi-instantaneous. Then a part of particles would be partially transformed, and this would lead, due to the difference in electronic properties of the γ- and α-phases, to the motion of electrons between CB of
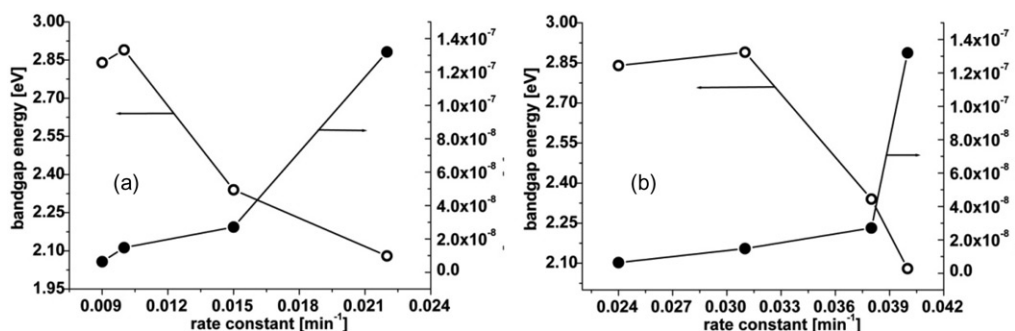
Figure 9. Correlation between the photogeneration rate and the electrical conductivity and band gap of synthesized materials for MB dye (a) and formaldehyde (b).

magnetite and hematite. The improvements of the charge separation and electron transport to the surface lead to increasing both the efficiency of the generation of hydroxyl radicals and the photocatalytic activity.

In general, by analyzing the photocatalytic properties of synthesized samples, we can see that there is a correlation between the photoactivity of materials and the electrical conductivity and the band gap (Fig. 9). The photocatalytic characteristics are better, when the electrical conductivity of the materials is higher, and the band gap width is smaller. It is shown that the dc electric conductivity is more important for the reaction rate comparatively to the phase composition and specific surface area (Fig. 9).

The observed effect is caused by an increase in the electron mobility, higher quantum efficiency of the photogeneration, and better separation of electron-hole pairs. An increase in the conductivity causes a growth of the electron mobility in the superficial layers of the photocatalyst and leads to an increase in the quantum efficiency and photoactivity. In this case, the number of $H^\bullet$ radicals and the performance of photo-degradation would be increased.

Conclusions

A new hydrothermal approach to the ultrafine iron oxides/hydroxides synthesis, which has permitted to obtain the materials with mesoporous structure and spherical particles, is proposed. The conductivity of synthesized materials is realized through the electron transfer mechanisms according to the non-Debye relaxation in the solid state, which is described by Jonscher's superlinear power law. The manifestation of quantum confinement effects has been recorded, which causes an increase in the width of the band gap of synthesized materials in comparison with voluminous materials. The correlation between the photodegradation constant rates, dc conductivities, and band gap is determined. An increase in the conductivity causes a growth of the electron mobility in the superficial layers of the photocatalyst and leads to an increase in the quantum efficiency and photoactivity of materials.

References

[1]   Golka, K., Kopps S., & Myslak Z. (2004). *Toxicol. Lett.*, 151, 203.

[2] Bahnemann, D. (2004). *Sol. Energy*, 77, 445.
[3] Kumar, S.G., & Devi, L. G. (2011). *J. Phys. Chem. A*, 115, 13211.
[4] Xiong, Y., Xie, Y., Chen, S., & Li, Z. (2003). *Chemistry-A European Journal*, 9, 4991.
[5] He, D., Chen, Y., Situ, Y., Zhong, L., & Huang, H. (2017). *Applied Surface Science*, 425, 862.
[6] Yuan, Z.Y., Ren, T. Z. & Su, B.L. (2004). *Catal. Today*, 93, 743.
[7] Benz, M., van der Kraan, A. M. & Prins, R. (1998). *Appl. Catal., A*. 172, 149.
[8] Zhang, Z. H. & Wang, P. (2012). *Energ. Environ. Sci.* 5, 6506.
[9] Fleet, M.E. (1986). *J. Solid State Chem.*, 62, 75.
[10] Cabot, A., Puntes, V.F., Shevchenko, E., Yin, Y., Balcells, L., Marcus, M. A., & Alivisatos, A.P. (2007). *J. Am. Chem. Soc.*, 129, 10358.
[11] Jung, K.-S. (2010) *Magnetite: Electrochemical Properties and Its Role in Flow Accelerated Corrosion*, N.Y.: Nova Sci.
[12] Cornell, R.M. *et al.* (2003). *The Iron Oxides: Structure, Properties, Reactions, Occurrences and Uses*, W.: Wiley-VCH.
[13] Jonscher, A.K. (1996). *Universal Relaxation Law*, London: Chelsea Dielectrics Press.
[14] Cheruku, R., Govindaraj, G., & Vijayan, L. (2014). *Mater. Chem. Phys.*,146, 389.
[15] Dyre, J.C. (2000). *Rev. Mod. Phys.*, 72, 873.
[16] Sei, J.O., Cook, D.C., & Townsend, H.E. (1998). *Hyperfine Interact.*, 112, 59.
[17] Kotsyubynsky, V., Ostafiychuk, B., Moklyak, V., & Hrubiak, A. (2015). *Solid State Phenom.*, 230, 120.
[18] Kotsyubynsky, V., Moklyak, V., & Hrubiak, A. (2014). *Mater. Sci.-Pol.*, 32, 481.
[19] Randhawa, B.S., Kaur, R., & Sweety, K. (1997). *J. Radioanal. Nucl. Chem.*, 220, 271.
[20] Kotsyubynsky, V.O., Grubiak, A.B., Moklyak, V.V., Pylypiv, V.M., & Lisovsky, R.P. (2014). *Metallofiz. Noveishie Tekhnol.,* 36, 1497.
[21] Ozdemir, O., Meydaneri, F., & Kariper, I. A. (2014). *Optoelectronics and Advanced Materials-Rapid Comm.*, 8, 727.
[22] Brus, L.E. (1983). *J. Chem. Phys.*, 79, 5566.
[23] Pradhan, G.K., & Parida, K.M. (2010). *International Journal of Engineering, Science and Technology*, 2, 53.
[24] Zhang, L.S., Wong, K.H., Zhang, D.Q., Hu, C., Yu, J.C., Chan, C.Y., & Wong, P.K. (2009). *Environ. Sci. Technol.*, 43, 7883.
[25] Hartmann, M., Kullmann, S. & Keller, H. (2010). *J. Mater. Chem.* 20, 9002.
[26] Xu, Z., Zhang, M., Wu, J., Liang, J., Zhou, L., & Lu, B. (2013). *Water Science and Technology*, 68, 2178.
[27] Leland, J. K., & Bard, A. J. (1987). *J. Phys. Chem*, 91, 5076.
[28] Mendili, Y., Bardeau, J. F., Randrianantoandro, N., Grasset, F., & Greneche, J. M. (2012). *J. Phys. Chem. C*, 116, 23785.